ELECTROCALORICS

A high-performance solid-state electrocaloric cooling system

Yunda Wang[1]*, Ziyang Zhang[1], Tomoyasu Usui[2], Michael Benedict[1], Sakyo Hirose[2], Joseph Lee[1], Jamie Kalb[1], David Schwartz[1]*

Electrocaloric (EC) cooling is an emerging technology that has broad potential to disrupt conventional air conditioning and refrigeration as well as electronics cooling applications. EC coolers can be highly efficient, solid state, and compact; have few moving parts; and contain no environmentally harmful or combustible refrigerants. We report a scalable, high-performance system architecture, demonstrated in a device that uses $PbSc_{0.5}Ta_{0.5}O_3$ EC multilayer ceramic capacitors fabricated in a manufacturing-compatible process. We obtained a system temperature span of 5.2°C and a maximum heat flux of 135 milliwatts per square centimeter. This measured heat flux is more than four times higher than other EC cooling demonstrations, and the temperature lift is among the highest for EC systems that use ceramic multilayer capacitors.

Over the two centuries since the invention of vapor compression, heat pumps have become an increasingly essential technology, with applications ranging from air conditioning and refrigeration to the stabilization of precision electronic components. Space cooling currently accounts for about 20% of the total electricity used in buildings and 10% of total electricity consumption around the world (*1*). As large countries continue to develop, the demand for air conditioning will increase. The global installation of room air conditioners is estimated to reach 4.5 billion units by 2050 (*2*). Applications extend beyond large-scale cooling, with efficient heat pumps being critical for thermal management of many electronic devices and sensors (*3*), including night-vision infrared sensors (*4*) and laser diodes (*5*).

Nevertheless, cooling technologies have only seen incremental changes in the past few decades. Vapor compression refrigeration, patented in 1803 (*6*), remains the predominant cooling technology in use. Vapor compression cooling has been difficult to displace because many decades of development have led to high efficiency, scalability, reliability, and relatively compact size (*7*). However, several issues suggest a need to move beyond this technology. The high-performance, nonflammable refrigerants commonly in use are hydrofluorocarbons (HFCs)—global-warming forcers typically thousands of times more potent than carbon dioxide (*8*). Phase-down of HFCs may be one part of a response to climate change. Replacement refrigerants require trade-offs between cost, efficiency, and safety (*9*). Trans-critical CO_2 systems have favorable thermodynamic properties but are incompatible with existing compressors and other equipment (*10*).

The inveteracy of vapor compression has hindered the development of zero–global warming potential (GWP) alternative technologies (*11*). High efficiency, characterized by the coefficient of performance (*COP*) (the heat pumping power divided by input power at a set operating temperature), is essential for addressing indirect CO_2 emissions associated with electricity consumption. Of non-vapor compression space-cooling technologies, only absorption coolers and evaporative coolers have achieved measurable market penetration, yet these are typically appropriate for specific-use cases or environments. Other technologies in development include those based on the thermoelectric effect (TE) (*12*), the magnetocaloric effect (*13*), the electrocaloric effect (ECE) (*14*, *15*), the elasto- and barocaloric

[1]PARC, A Xerox Company, 3333 Coyote Hill Rd., Palo Alto, CA 94304, USA. [2]Murata Manufacturing Co., Ltd., 1-10-1, Higashikotari, Nagaokakyo, Kyoto 617-8555, Japan.
*Corresponding author. Email: yundaw@parc.com (Y.W.); dschwart@parc.com (D.S.)

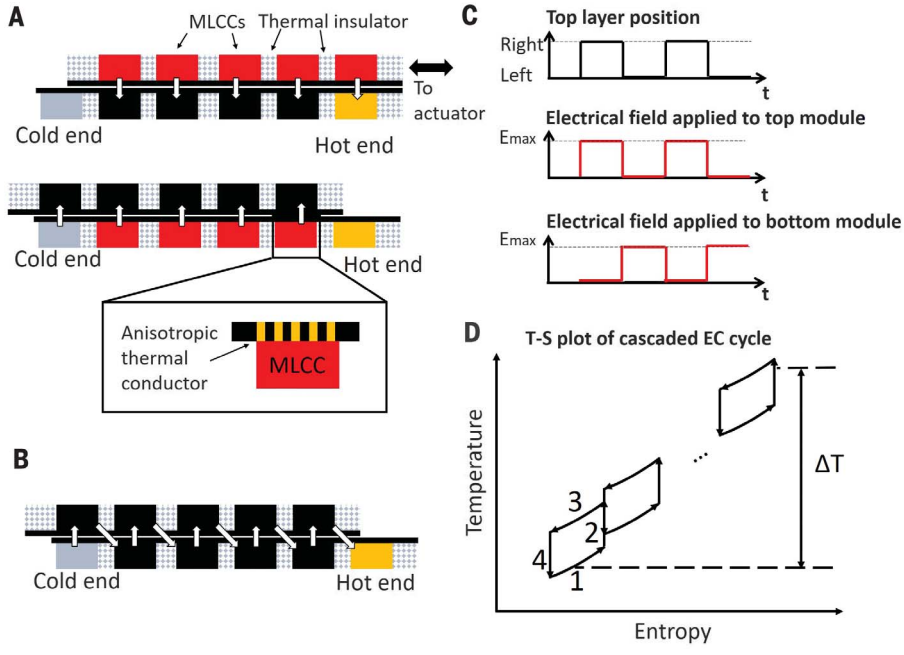

Fig. 1. Operation of the EC system. (**A**) Relative positions of the EC modules in the two heat transfer stages. (**B**) The heat flow path. (**C**) Time-domain illustration of the cyclic application of electric field and actuation. E_{max}, The maximum electric field applied to the module; t, time. (**D**) Schematic of the Brayton cycle as observed for each MLCC. Stage 1 is a cold isoelectric stage. The electric field across the MLCC is low, the MLCC absorbs heat from an adjacent MLCC in the opposite module, and both temperature and entropy increase. Stage 2 is a nominally adiabatic stage. The electric field across the MLCC is increased, resulting in an ECE-induced temperature increase of the MLCC; at the same time, the actuator voltage is switched so that the MLCC module alignment shifts. This stage is ideally isentropic. Stage 3 is a hot isoelectric stage. With the electric field still high, the MLCC rejects heat to the adjacent MLCC of the opposite module; both temperature and entropy decrease. Stage 4 is a nominally adiabatic stage. The electric field is switched back to zero, leading to a temperature decrease in the MLCC; the actuator is switched so that the MLCCs return to their original alignment. This stage is ideally isentropic. T-S, temperature-entropy.

effects (*16*), adsorption cooling (*17*), and enhanced radiative cooling (*18*). Gas-phase technologies, including Stirling and thermoacoustic coolers, have found niche applications, for example, in cryogenic pulse-tube refrigerators. The only technology that has been widely commercialized is based on the TE, primarily as Peltier devices for electronics cooling. The success of TE technology is directly attributable to its compact form factor and simple operation. Despite decades of intensive research, the low efficiency of TE commercial devices arises from fundamental material and form-factor limitations, which have not been substantially improved. There appears to be no clear path to achieving vapor compression–equivalent efficiencies, especially for larger-scale systems (*19*).

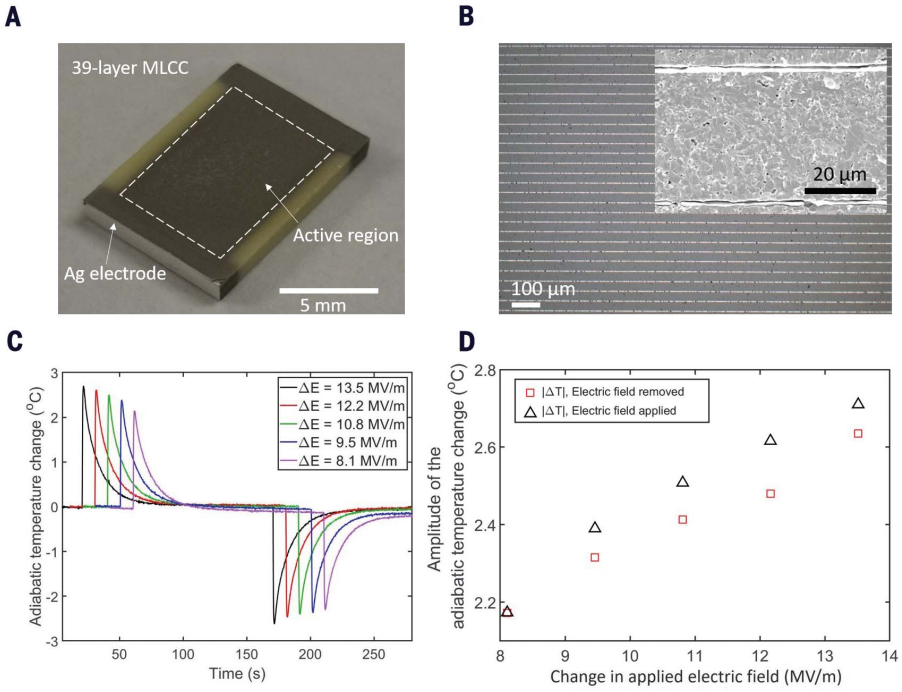

Fig. 2. MLCC images and characterization results. (**A**) Photograph of an MLCC. (**B**) Photograph and SEM (inset) of a cross section of an MLCC. (**C**) Induced temperature changes of the MLCC over time with the application and removal of polarizing electric fields. Measurements are performed at room temperature. ΔE, change in applied electric field. (**D**) Amplitude of the temperature changes during heating and cooling as a function of electric field magnitude.

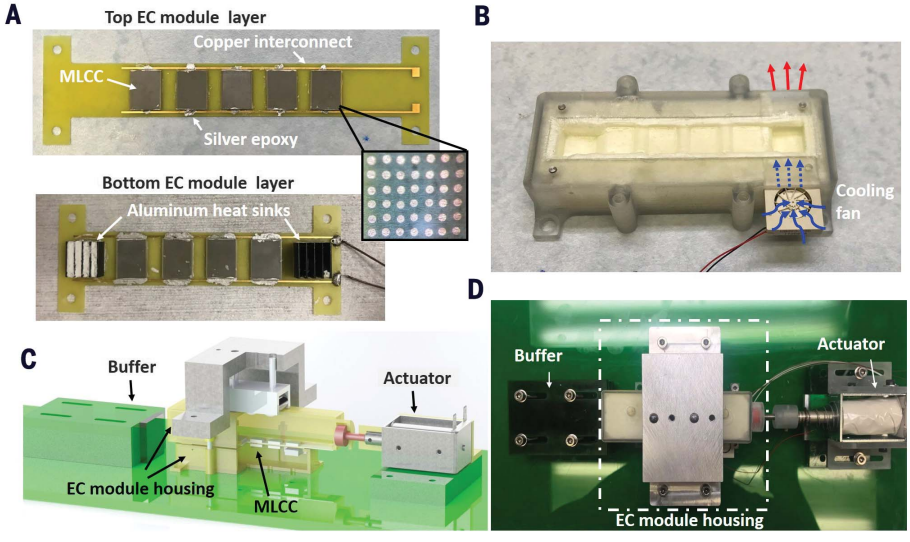

Fig. 3. EC cooler and key components. (**A**) Top and bottom EC modules assembled on ATC plates. The inset shows the copper through-vias behind the MLCCs. (**B**) Bottom housing structure, including miniature fan and air flow path. (**C**) Solid model of the cooler assembly. (**D**) Photograph of the cooler assembly.

Among emerging technologies, electrocaloric (EC) cooling has the potential for high efficiency and near solid-state operation. The ECE is a material property characterized by an adiabatic temperature change with an applied electric field (*20*). A heat pump can be realized by thermally coupling EC materials alternately to a heat sink and source synchronously with the application and removal of a polarizing field. The ECE is driven by electric fields, eliminating the need for large compressors, pumps, or magnets. The strategy is a scalable replacement, both for vapor compression systems and for thermoelectric devices (*21*–*24*). In recent decades, tremendous progress has been made in material development, yielding extremely promising materials that evince a "giant" ECE associated with a first- or second-order ferroelectric phase change. Both high-performing relaxor ferroelectric ceramic (*14*, *25*–*30*) and polymer EC materials (*15*, *27*, *28*) have been developed. Predictions of adiabatic temperature changes greater than 40°C were based on extrapolations from laboratory measurements (*27*). Nevertheless, demonstrations of cooling systems based on advanced materials have lagged. The primary limitation has been the inability to realize these materials in scalable form factors at quantities compatible with incorporation into systems. Material properties have been characterized in thin films and small bulk samples in laboratories. Achieving similar properties in components with high thermal mass has remained elusive. Most system demonstrations (*31*–*38*) have low temperature lifts, and only a few reported measured cooling power (*31*, *32*). Polymer and ceramic materials have similar volumetric EC energy densities, and systems with both material types have been demonstrated. The highest temperature span of a polymer system reported in a peer-reviewed publication is 5 K (*34*). A temperature span up to 8.4°C of a polymer system was claimed in a government project report (*39*). However, the low thermal conductivity of polymers necessitates the use of thin films of not more than several tens of micrometers for adequate heat transfer for a practical heat pump [for example, (*31*)]. This makes scaling to high-capacity and high-performance systems very challenging. Ceramic materials have higher thermal conductivity, enabling thicker, higher–thermal mass devices.

We developed a scalable, high-performance system based on ceramic EC materials in a

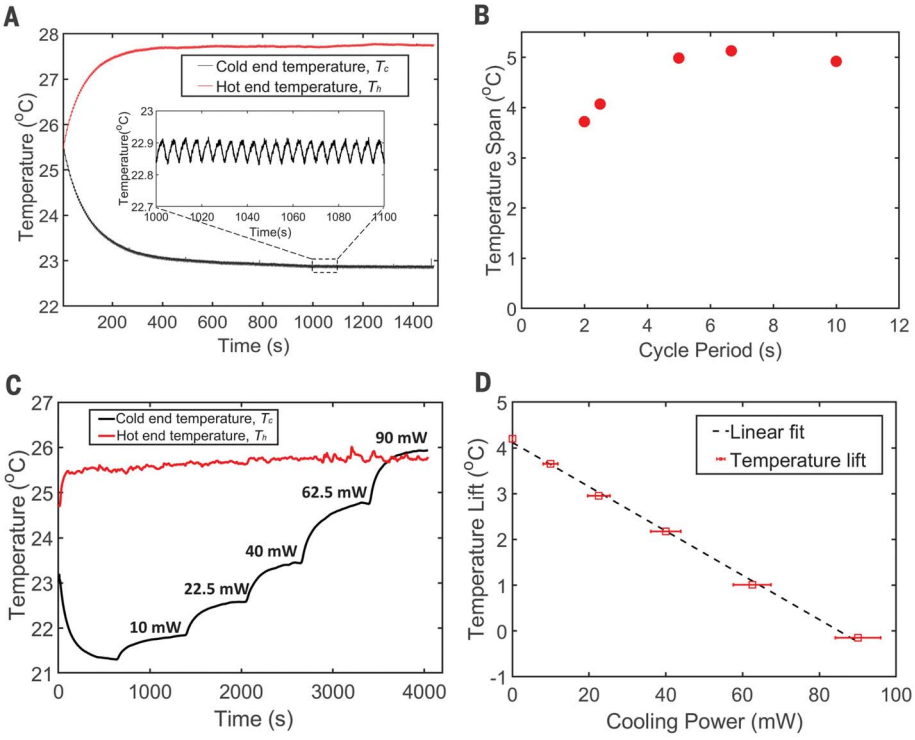

Fig. 4. Characterization result of the EC cooler. (**A**) Measured hot- and cold-end temperatures with a 400-V polarizing voltage and 5-s cycle period. Data are sampled at 20 Hz. (**B**) The maximum temperature span as a function of operating cycle period with 400-V operation. (**C**) Measured hot- and cold-end temperatures at different applied heater powers. Data are sampled at 20 Hz and filtered by a 200-point moving average. (**D**) System temperature lift, $T_h - T_c$, as a function of cooling power. Error bars show the maximum value range based on the calculated uncertainty in the heater power measurement.

modular cascaded self-regenerating architecture with low thermal loss. We demonstrated the system in a device that uses partially ordered $PbSc_{0.5}Ta_{0.5}O_3$ (PST)–based EC multilayer ceramic capacitors (MLCCs) as the working elements. These MLCCs have an adiabatic temperature change of 2.5°C for a polarizing field of 10.8 MV/m at room temperature. The system achieves a temperature span of 5.2°C and a heat flux of 135 mW/cm^2 separately, using the same polarizing field. This temperature span is one of the highest reported in a ceramic EC system since the foundational work at the Moscow Power Engineering Institute in the early 1990s (*29*, *30*). The fluid-regenerated systems built there used 0.3-mm-thick PST plates as the working body and reported a temperature lift as high as 12.7°C (*30*). Unlike that early work, which was designed as a laboratory experiment, we designed our system to be scalable, using multilayer capacitors fabricated in an electronics manufacturing process, a modular configuration, and solid-state regeneration. With a few exceptions (*31*, *32*), most EC device reports only include measurements of maximum temperature span and do not measure cooling capacity. This is a critical quantity for technology comparison. For EC systems, heat flux gives insight into material utilization and overall system size. Our measured heat flux is ~4.5 times the 29.7 mW/cm^2 that was reported for a system that achieved a maximum temperature span of 2.8°C at zero heat flux in a separate experiment (*31*). Scalable materials, together with mechanical simplicity and modular design, can ultimately enable a system whose size, efficiency, and cost are competitive with those of vapor compression.

Our system comprises a pair of stacked modules, each containing EC MLCCs distanced with thermal insulating materials between them (Fig. 1, A and B). The inclusion of the insulation is a critical improvement of this design over continuous active regenerators because it interrupts the thermal shunting along the temperature gradient, a substantial source of loss. The modules are thermally coupled such that heat is easily transferred from one to the other. They are moved laterally relative to one another as the polarizing electric field is switched synchronously (Fig. 1C). In this way, we generated a temperature lift between the two ends of the device that is greater than the MLCC adiabatic temperature change. Another key design innovation is the use of anisotropically thermally conductive (ATC) plates to enhance heat exchange between layers while maintaining low lateral thermal leakage. The ATC plates are designed to have high through-plane and low in-plane thermal conductivity.

We prepared the EC MLCCs using a solid-state reaction and tape casting process (*40*, *41*), a large-volume capacitor manufacturing method commonly used in the electronics industry. We formed the dielectric layer from PST EC material with a B-site cation order of ~0.70 to 0.78. The Curie temperature of this material is 13°C and can be readily modified with chemical substitution and by controlling B-site cation ordering (*42*). The inner electrodes are Pt. The dielectric and electrode layers are ~37- and ~1.5-μm thick, respectively. We used Ag paste to form the external terminals. We photographed and obtained a scanning electron microscopy (SEM) image of an MLCC cross section (Fig. 2, A and B). We characterized the adiabatic temperature change of the MLCC by direct measurement. We measured the dynamic EC temperature as the polarizing fields are applied and removed (Fig. 2C). We also measured the heating and cooling adiabatic temperature changes of the MLCC for several magnitudes of the polarizing field (Fig. 2D) (*43*).

We optimized the system to maximize heat transfer between the MLCC modules while minimizing thermal leakage (Fig. 3, C and D). We fabricated each ATC plate from glass-reinforced epoxy (FR-4) laminates and copper in a standard commercial printed circuit board (PCB) process. In the regions of the plate where the MLCCs are attached, plated-copper through-vias serve as thermal shunts for high through-plane thermal conductivity. The diameter of the vias and the pitch of the array are 150 and 300 μm, respectively. The effective through-plane thermal conductivity in the region of the vias is about 85.7 W/(m·K) based on a finite-element simulation in COMSOL, assuming 400 W/(m·K) as the thermal conductivity of electroplated copper and 0.29 and 0.81 W/(m·K), respectively, as the through-plane and in-plane thermal conductivities of FR-4 (*44*). The MLCCs are assembled onto the ATC plates to form the top and bottom EC modules (Fig. 3A), which contained five and four MLCCs, respectively. The bottom module has an aluminum plate-fin heat sink at each end to facilitate achieving stable temperatures when required. The modules are seated in a 3D-printed VeroClear housing filled with polyurethane foam insulation with a thermal conductivity of 0.04 W/(m·K). The housing (Fig. 3B) provides structural support and minimizes heat leakage. We attached a miniature fan to one end to flow air across the hot-end heat sink. We connected the top housing to a spring-returned single-acting linear solenoid

actuator with a maximum stroke length of 12.7 mm and a contraction force of 7.2 N at 50% stroke. Application of 12-V dc to the actuator draws the top module toward the actuator. When the voltage is returned to zero, the solenoid relaxes and a spring returns it to its original position. The extents of actuation in each direction are set by adjusting the position of the actuator and an adjustable buffer. The EC module housing provides vertical pressure through a set of wheels to enhance the thermal contact between the two modules without hindering sliding. Control software synchronizes the actuation of the top module layer with the application of electric fields to the EC capacitors (*43*).

We operated the MLCCs under an EC Brayton cycle, with two isoelectric and two isentropic stages (Fig. 1D). To measure the maximum temperature span, we fully insulated both ends of the device. The heat sinks are filled with silicon paste to prevent air flow, the fan is removed, and the hot end is enclosed in foam insulation. Thermistors for measurement of the hot and cold end temperatures, T_h and T_c, respectively, were fitted into bore holes in the aluminum heat sinks. The variation in offset between the two thermistors was measured to be less than 0.1°C, allowing accurate measurement of small temperature lifts. We measured hot-end and cold-end temperatures with the cooler operated at a 400-V polarizing voltage (equivalent to ~10.5-MV/m electric field) and a 0.2-Hz switching frequency (5-s period) with a 50% duty cycle and negligible transition time (Fig. 4A). We also determined the maximum temperature lift $\Delta T = T_h - T_c$ for several different operating cycle periods, all with a polarizing voltage of 400 V (Fig. 4B). We achieved a maximum temperature span of 5.2°C at an operation frequency of 0.15 Hz (6.7-s period). This is equivalent to a ~0.09°C/mm temperature gradient along the heat pumping axis.

To measure the cooling power, we attached a 1-mm–by–2-mm 100-ohm chip resistor to the cold end and used it as an electric heater. The fan provides air flow across the uninsulated hot-end heat sink to maintain T_h near ambient temperature. We characterized the system by varying the current through the heater resistor and allowing the temperature lift ΔT to stabilize (Fig. 4, C and D). Because the coupling to ambient temperature is imperfect, over the course of the experiments, the heat sink temperature, T_h, increases slightly as heat is pumped to the hot end. The cold end temperature, T_c, changes in discrete steps as the heater power is varied. Because the temperature difference between the heater and the environment is small and the insulation is very good, heat leakage is negligible, and the heat pumped by the cooler is well approximated by the applied heater power. The measurement results show a linear relationship between the cooling power and temperature lift. We achieved a maximum heat power of ~85 mW with no temperature lift. This value is equivalent to a heat flux of ~135 mW/cm^2, given the 0.63-cm^2 active cooling area of the MLCC. The specific cooling power normalized to the volume of the active electrocaloric material is ~116 mW/cm^3. We also calculated the cooling power normalized to the total volume and to the total mass—each including the inactive material of the MLCC, the ATC plate, and the insulating material—to be ~29.2 mW/cm^3 and ~6.8 mW/g, respectively. The equivalent heat flux in the heat pumping direction is ~156 mW/cm^2, given the 0.54-cm^2 cross-sectional area normal to the heat flow direction.

A key determinant of the efficiency of a heat switch–based EC cooling system is the effective thermal contrast ratio K', defined as the ratio of "effective" on and off conductivity, k_h' and k_l' (*45*). We can model our system as a cascaded heat switch–based architecture (*43*). In an otherwise ideal heat switch–based system operating under a Carnot cycle, the *COP* is given by

$$COP_{K'} = \frac{Q_c}{W_{ECE}} = COP_{r,K'} \cdot COP_{Car} = \left(\frac{\sqrt{K'}-1}{\sqrt{K'}+1}\right)^2 COP_{Car} \quad (1)$$

where W_{ECE} is the work required to move heat through actuation of the ECE, K' is the effective heat-switch contrast ratio, Q_c is the heat collected from the cold side of the device, and $COP_{Car} = T_c/(T_h - T_c)$ is the maximum thermodynamic (Carnot) *COP*. $COP_{r,K'}$ is the maximum *COP* relative to COP_{Car} for a heat switch–based system with effective thermal contrast ratio K' (*33*). Assuming a necessarily imperfect charge recovery, system efficiency is given by

$$COP_C = Q_c/W_{tot} = Q_c/[W_{ECE} + W_{elec}(1-\eta_{ECR})] = \eta_{elec} \cdot COP_{K'} \quad (2)$$

where W_{elec} is the additional electrical work associated with charging and discharging the EC capacitor, and η_{ECR} is the electrical charge recovery (ECR) efficiency, or the portion of electrical energy recovered each cycle. This work is often disregarded in thermodynamic-cycle efficiency calculations that assume that input work and net cycle work are equivalent, leading to unrealistically high efficiency estimates. We did not observe measurable frictional or Joule heating in the system. Additionally, the mechanical work required to move the reciprocating system is orders of magnitude smaller than other work terms (*43*). Thus, we can neglect this term as well as the electrical work required to drive the actuator, assuming a reasonably efficient actuator. The electrical efficiency factor η_{elec} is given by

$$\eta_{elec} = \frac{W_{ECE}}{W_{ECE} + W_{elec}(1-\eta_{ECR})} \quad (3)$$

and can be approximated as

$$\eta_{elec} = \frac{1}{1 + \frac{T\varepsilon}{\rho c_E}\left(\frac{\Delta E}{\Delta T}\right)^2 (1-\eta_{ECR})} \quad (4)$$

for given electrical permittivity ε, material density ρ, and heat capacity at constant electric field c_E (*43*). As detailed in (*43*), this approximation is based on a number of simplifying assumptions to allow analytical insight. A more complete thermodynamic model is required for an accurate calculation of η_{elec} and system *COP* (*46*). Operating on a Brayton cycle instead of a Carnot cycle, the *COP* is reduced by the ratio of the temperature difference between the heat source and heat sink to the maximum temperature difference internal to the device, Δ/δ (*45*), giving the system relative *COP* (sometimes termed efficiency):

$$COP_r = \frac{\Delta}{\delta} \cdot \frac{COP_C}{COP_{Car}} = \frac{\Delta}{\delta} \frac{1}{1 + \frac{T\varepsilon}{\rho c_E}\left(\frac{\Delta E}{\Delta T}\right)^2 (1-\eta_{ECR})} \left(\frac{\sqrt{K'}-1}{\sqrt{K'}+1}\right)^2 \quad (5)$$

We determined η_{elec} as a function of η_{ECR} for the partially ordered PST material used in this work (fig. S5) and the material parameters (table S2). As the material ECE improves relative to the permittivity, the impact of ECR decreases. A simple tank circuit can achieve η_{ECR} as high as 98% in the best case (*47*). This value would yield an electrical efficiency factor of 77.3%. With a more conservative η_{ECR} of 95%, the electrical efficiency factor is 57.7%.

In our system, the thermal contrast ratio K' was calculated to be 6.7 (*43*), corresponding to a $COP_{K'}$ of 20% and a potential COP_r of 11.5% in the limit of $\Delta/\delta = 1$, assuming 95% effective charge recovery, and a potential COP_r of 15.5% with 98% charge recovery efficiency, based on a simple, linearized efficiency model. This value is itself competitive with thermoelectric cooling devices, which typically are limited to COP_r < 15% (*48*). Although the thermal contrast ratio of 6.7 is notably smaller than the 27 previously reported by our team (*32*), the previous result was for a single-stage silicon heat switch–based system that is not readily scalable to high temperature lifts. The low thermal contrast ratio in the present system is largely attributable to low "off" conductance associated with the high thermal conductance of the thick copper traces

used. We anticipate being able to achieve a contrast ratio of 23 (table S3) through improved metallization design. Much higher efficiencies are possible with increased K' through straightforward system improvements. These include the following: (i) Reducing the thickness of the copper traces, t_m, on the PCB from 36 to 1 μm. Sputtered ~1-μm-thick copper traces have been experimentally verified to carry the transient switching current. (ii) Replacing the PCB with a polymer material like acrylic. Polymers have much lower thermal conductivity [~0.2 W/(m·K)] than the in-plane thermal conductivity of FR-4 [0.81 W/(m·K)]. (iii) Improving the MLCC form factor. MLCCs of the type used in this device have higher thermal conductivity in the direction parallel to the metal inner electrodes (*49*), yet this value is constrained to be normal to the preferred heat transfer direction in the reported device because of the relatively few layers and large area of the MLCCs used. If the PST MLCCs are fabricated with the same form factor as a commercial MLCC (1210ZG226ZAT2A, AVX, Northern Ireland) and assembled into the system (see fig. S6), the performance can be substantially enhanced. Further improvements are also possible, for example, by using a higher-conductivity metal for electrodes. Our estimate of the COP_r of the current design, along with assumptions of these improvements for η_{ECR} of 95 and 98%, shows that up to 56.4% may be achievable with the existing PST material (table S3). These values could make our system competitive with vapor compression cooling.

REFERENCES AND NOTES

1. International Energy Agency (IEA), "The future of cooling: Opportunities for energy efficient air conditioning" (Report, IEA, 2018).
2. S. Sneha, I. Campbell, A Kalanki, "Solving the global cooling challenge: How to counter the climate threat from room air conditioners" (Report, Rocky Mountain Institute, 2018).
3. S. Trutassanawin, A. Eckhard, paper presented at the International Refrigeration and Air Conditioning Conference, paper R172, Purdue University, West Lafayette, IN, 2004.
4. J. S. Lewis, N. K. Dhar, L. A. Elizondo, R. Dat, *Proc. SPIE* **9609**, 960902 (2015).
5. H. J. Lee, J. S. Yoon, C.-J. Kim, *Heat Transf. Asian Res.* **30**, 357–370 (2001).
6. T. Moore, *An Essay on the Most Eligible Construction of Ice-houses: Also, a Description of the Newly Invented Machine Called the Refrigerator* (Bonsal & Niles, 1803).
7. W. Goetzler, R. Zogg, J. Young, C. Johnson, "Energy savings potential and RD&D opportunities for non-vapor-compression HVAC technologies" (Report, U.S. Department of Energy, 2014).
8. The United Nations Environment Programme (UNEP), "2010 Report of the Refrigeration, Air Conditioning and Heat Pumps Technical Options Committee (RTOC). Montreal protocol on substances that deplete the ozone layer" (UNEP, 2011).
9. W. Goetzler, R. Zogg, J. Young, C. Johnson, *ASHRAE J.* **56**, 12–23 (2014).
10. P. Nekså, H. T. Walnum, A. Hafner, paper presented at the Ninth IIR Gustav Lorentzen Conference on Natural Working Fluids (GL 2010), Sydney, Australia, 12 to 14 April 2010.
11. J. Shi *et al*., *Joule* **3**, 1200–1225 (2019).
12. B. Russ, A. Glaudell, J. J. Urban, M. L. Chabinyc, R. A. Segalman, *Nat. Rev. Mater.* **1**, 16050 (2016).
13. V. Franco *et al*., *Prog. Mater. Sci.* **93**, 112–232 (2018).
14. A. S. Mischenko, Q. Zhang, J. F. Scott, R. W. Whatmore, N. D. Mathur, *Science* **311**, 1270–1271 (2006).
15. B. Neese *et al*., *Science* **321**, 821–823 (2008).
16. J. Tušek *et al*., *Nat. Energy* **1**, 16134 (2016).
17. Y. Tu, R. Wang, Y. Zhang, J. Wang, *Joule* **2**, 1452–1475 (2018).
18. Y. Zhai *et al*., *Science* **355**, 1062–1066 (2017).
19. J. W. Peeples, *Electronics Cooling Magazine* **7**, 16–24 (2001).
20. I. Kriaa, N. Abdelmoula, A. Maalej, H. Khemakhem, *J. Electron. Mater.* **44**, 4852–4856 (2015).
21. S. Pandya *et al*., *Phys. Rev. Appl.* **7**, 034025 (2017).
22. M. Valant, *Prog. Mater. Sci.* **57**, 980–1009 (2012).
23. S. Lu, Q. Zhang, *Adv. Mater.* **21**, 1983–1987 (2009).
24. S. Patel, A. Chauhan, R. Vaish, *Energy Technol.* **4**, 1097–1105 (2016).
25. Y. Hou, L. Yang, X. Qian, T. Zhang, Q. M. Zhang, *Philos. Trans. R. Soc. London Ser. A* **374**, 20160055 (2016).
26. Y. Hou, L. Yang, X. Qian, T. Zhang, Q. M. Zhang, *Appl. Phys. Lett.* **108**, 133501 (2016).
27. S. G. Lu *et al*., *Appl. Phys. Lett.* **97**, 162904 (2010).
28. X. Li *et al*., *J. Mater. Chem. C* **1**, 23–37 (2013).
29. Y. V. Sinyavsky, V. Brodyansky, *Ferroelectrics* **131**, 321–325 (1992).
30. Y. V. Sinyavskii, *Chem. Petrol. Eng.* **31**, 295–306 (1995).
31. R. Ma *et al*., *Science* **357**, 1130–1134 (2017).
32. Y. D. Wang *et al*., *Appl. Phys. Lett.* **107**, 134103 (2015).
33. R. Epstein, K. Malloy, *J. Appl. Phys.* **106**, 064509 (2009).
34. H. Gu *et al*., *Appl. Phys. Lett.* **102**, 122904 (2013).
35. T. Zhang, X.-S. Qian, H. Gu, Y. Hou, Q. M. Zhang, *Appl. Phys. Lett.* **110**, 243503 (2017).
36. H. Gu, X. S. Qian, H. J. Ye, Q. M. Zhang, *Appl. Phys. Lett.* **105**, 162905 (2014).
37. U. Plaznik *et al*., *Appl. Phys. Lett.* **106**, 043903 (2015).
38. Y. D. Wang *et al*., paper presented at the Eighth International Conference on Caloric Cooling (Thermag VIII), Darmstadt, Germany, 16 to 20 September 2018.
39. S. R. Annapragada, P. Verma, A. Sur, W. Xie, "High-efficiency solid-state heat pump module" (Project Final Report, U.S. Department of Energy, 2018).
40. S. Hirose *et al*., *APL Mater.* **4**, 064105 (2016).
41. B. Nair *et al*., *Nature* **575**, 468–472 (2019).
42. N. Setter, L. E. Cross, *J. Appl. Phys.* **51**, 4356–4360 (1980).
43. Materials and methods are available as supplementary materials.
44. K. Azar, J. E. Graebner, in *Proceedings of the 12th IEEE SEMI-THERM Symposium* (IEEE, 1996), pp. 169–182.
45. S. J. Smullin, Y. D. Wang, D. E. Schwartz, *Appl. Phys. Lett.* **107**, 093903 (2015).
46. J. Gong, A. J. H. McGaughey, *Int. J. Energy Res.* **44**, 5343–5359 (2020).
47. E. Defay *et al*., *Nat. Commun.* **9**, 1827 (2018).
48. M. K. Rawat, H. Chattopadhyay, S. Neogi, *Int. J. Emerg. Technol. Adv. Eng.* **3**, 362–367 (2013).
49. S. Kar-Narayan, N. D. Mathur, *Appl. Phys. Lett.* **95**, 242903 (2009).

ACKNOWLEDGMENTS

We thank Q. Wang at PARC for his support on microfabrication and also C. Minami, N. Furusawa, Y. Inoue, and K. Honda for their kind assistance in fabricating MLCCs. **Funding:** PARC and Murata internal research funding. **Author contributions:** Y.W., D.S., and M.B. conceived and designed the system. Z.Z., M.B., J.K., J.L., and Y.W. fabricated the prototype. Z.Z. performed the experiments. T.U. and S.H. fabricated and tested the MLCCs. D.S. performed the thermodynamic analysis. Y.W., D.S., Z.Z., and M.B. organized the data and wrote the manuscript. All authors reviewed the manuscript. **Competing interests:** D.S. and Y.W. are inventors of U.S. patent application serial number 15/375,713, which claims the major features of the cascaded self-regenerating design. **Data and materials availability:** All data are available in the manuscript or the supplementary materials.

SUPPLEMENTARY MATERIALS

science.sciencemag.org/content/370/6512/129/suppl/DC1
Materials and Methods
Figs. S1 to S6
Tables S1 to S3
References

8 December 2019; resubmitted 7 May 2020
Accepted 12 August 2020
10.1126/science.aba2648

A high-performance solid-state electrocaloric cooling system

Yunda Wang, Ziyang Zhang, Tomoyasu Usui, Michael Benedict, Sakyo Hirose, Joseph Lee, Jamie Kalb and David Schwartz

Science **370** (6512), 129-133.
DOI: 10.1126/science.aba2648

Competitive cooling with capacitors

Current large-scale cooling devices use vapor compression refrigeration. The efficiency of air conditioners has been optimized, but they can be noisy and rely on problematic greenhouse gases. Two groups now present designs for electrocaloric cooling using lead scandium tantalate capacitors that change temperature under an electric field. Y. Wang *et al.* obtained a very large heat flux using only solid materials and a cooling fan to remove heat from their device. Torello *et al.* used fluids for heat transfer, leading to a very large temperature difference between the hot side and the cold side. The new designs demonstrate the potential for devices that might be competitive with vapor compression–based appliances with further optimization.

Science, this issue p. 129, p. 125